PNAS
www.pnas.org

Supplementary Information for

Gain-of-Function Mutations in a Member of the Src Family Kinases Cause Autoinflammatory Bone Disease in Mice and Humans

Koichiro Abe[a,1,*], Allison Cox[b,1], Nobuhiko Takamatsu[c], Gabriel Velez[d,e], Ronald M. Laxer[f], Shirley M.L. Tse[f], Vinit B. Mahajan[d], Alexander G. Bassuk[b], Helmut Fuchs[g], Polly J. Ferguson[b,2] & Martin Hrabě de Angelis[g,h,i,2]

Koichiro Abe
Email: abeko@is.icc.u-tokai.ac.jp

This PDF file includes:

Supplementary text
Figs. S1 to S7
Tables S1 to S4
References for SI reference citations

www.pnas.org/cgi/doi/10.1073/pnas.1819825116

Supplementary Information

Main Text

Results and Discussion

Structural modeling of mutated FGR proteins. We have used structural modeling to help determine the pathogenicity of gene mutations (1-3), and did so for the FGR mutants. Crystal structures for SRC, both in its active and inactive form, have been solved (4). We generated three-dimensional models of FGR using these structures as templates (*SI Appendix,* Fig. S4 and S6).

The *de novo* Arg118Trp mutation removes a positive charge near the distal loop of the SH3 domain, a domain involved in mediating peptide bonding and protein-protein interactions (5) (*SI Appendix,* Fig. S4*A*). We ran all-atom molecular dynamics simulations of the wild-type and p.Arg188Trp SH3 domains using the AMBER14 force field for 100-ns each (*SI Appendix,* Fig. S5). Superimposition of the final structures

obtained during this 100-ns simulation showed that the p.Arg118Trp disrupts a hydrogen bonding interaction with the neighboring Thr125 residue (*SI Appendix,* Fig. S4*C*). In the SRC inactive state the SH3-SH2 domain forms a hinge that is in the closed conformation (4). During activation, the SH3 and SH2 domain unlatch from the C-terminal portion of the protein, making Tyr416 open for phosphorylation (*SI Appendix,* Fig. S4*A*). Disruption of this interaction may destabilize the protein, either enhancing autophosphorylation or preventing C-terminal phosphorylation by Csk.

The Pro525Ser mutation is located on the C-terminal tail of the FGR structure. The C-terminal tail is a critical regulatory region of the protein, and thus, its composition is highly conserved (*SI Appendix,* Fig. S6*B*). Phosphorylation of Tyr523 by Csk inactivates the enzyme by keeping it in its closed conformation. This prevents ulterior phosphorylation of Tyr412, which is important to form its open active confirmation (4). In the closed conformation, the C-terminal region binds to two hydrophobic pockets of the SH2 domain (6). Phosphorylated Tyr523 binds to the N-terminal hydrophobic pocket specifically, and the following three amino acid residues are important for this binding (6). The surface of the pocket is neutral in charge by hydrophobic residues

positioned in SH2. Thus, it is expected that the Pro525Ser mutation prevent the hydrophobic interactions within the pocket, leading to instability to form the closed confirmation (*SI Appendix,* Fig. S6*A*). Thus, it is suggested that the Pro525Ser mutation causes abnormal activation–inactivation cycles of FGR protein. This could lead to constitutive activation of FGR as observed in the *Ali18* mouse.

Methods

Whole genome sequencing (WGS) by next generation sequencer (NGS).

Genomic DNA for WGS was extracted from *Ali18/+* and wild type kidney using QIAGEN genome tip by manufactures protocol. Briefly, the frozen kidneys were crushed by Cryo-Press (MICROTEC CO., LTD, Chiba, Japan), and then crushed powder was used for column separation. The quality of genomic DNA was assessed by Victor 3 fluorometry and gel electrophoresis, and the library construction and HiSeq NGS were ordered to Macrogen Japan (http://www.macrogen-japan.co.jp/). The sequence data were analyzed by IGV (http://software.broadinstitute.org).

Genotyping of *Ali18* mice. The MIT microsatellite markers used for genetic mapping are described previously (7, 8). The D4Neu12 and D4Neu6 markers were originally made using microsatellite sequences detected in the critical region of Mouse Genome sequence database; D4Neu12-L, 5'-CTGGGTCTTCAGAGCTACGTC; D4Neu12-

R, 5’-GATCTGAGGACTGTGGGGAT; D4Neu6-L, 5’-CTCCTGATTCCATTGCAGTG; D4Neu6-R, 5’-CTATGTAGTCAGAGCTGTCCTGG.

After sequence detection of the p.Asp502Gly mutation, we continue to use the PCR primer pair of the exon of the *Fgr* gene for *Ali18* genotyping. Genomic PCR was performed using the following oligonucleotides spanning exon12 to exon13 of the *Fgr* gene: Fgr_ex10-11L, 5’-TTAATCCAGCAGTTCCCAGG and Fgr_ex10-11R, 5’-GGGATTGGCAAGAGCAAG. The PCR products were directly digested with the Mbo II restriction enzyme (NEB). MboII specifically recognizes wild type (5’-GAAGA-3’) but not *Ali18* (5’-GAAGG-3’) sequences in the PCR products.

For genotyping of F0 and F1 mice produced by genome editing, we sequenced PCR products of exon 3 of the *Fgr* gene around the translational initiation site using the following oligonucleotides: Fgr_ex1L, 5’-TAGTGGTACACCAGCCAGGG, and Fgr_ex1R, 5’-CGTTGAGCTAGAGAATAGAGCTG. In addition, PCR-based genotyping of F0 mice was performed for the $Fgr^{Asp502Gly}$ mutation described above.

Histology and bone inflammation scoring. Hind paws were sectioned by standard histological procedure with formic acid decalcification as described previously (9). Bone inflammation was scored for each bone of feet (talus, calcaneus, navicular bone, cuneiform bone, metatarsal bone, and phalanx) according to the percentage of the bone marrow space containing inflammatory cells; 0 (no inflammation), 1 (< 25%), 2 (25-75%), and 3 (>75%). The bone inflammation scores were then averaged for each F1 animals.

Protein preparation from tissues and transfection. Protein samples were prepared from tissues of *Ali18/+* and *Ali18/Ali18* mice. Tissues were once frozen, and then used for making tissue powder by Cryo-Press (MICROTEC CO., LTD, Chiba, Japan). Bone marrow was flushed from femur, and put through nylon mesh; the cells were centrifuged and used for protein preparation. Protein extract was dissolved with buffer containing 1x complete protease inhibitor cocktail (Roche) and 1x phosphatase inhibitor cocktail (Nacalai tesque, Japan), and sonicated for 10 minutes. Plasmid DNA described in *SI Appendix*, Methods, was transfected into the NIH3T3 cells using the

FuGENE reagent (Roche diagnostics). After 72 hours from transfection, cells were harvested for protein preparation as described above.

Protein phosphorylation assays. Phosphorylation of Eno1 by Fgr, FGR or their mutants was analyzed according to Bagheri-Yarmand *et al.* (10) with slight modifications. One and half μg of GST-Eno1 with 4 μl of *in vitro* transcription/translation reaction of Flag-Fgr or its mutant, or 50 ng of GST-FGR or its mutants were suspended in 15 μl of kinase buffer [20 mM Hepes, pH 7.6, 10 mM MgCl2, 1 mM beta-glycerolphosphate, 2.5 mM NaF, 1 mM Na3VO4, 1 mM DTT] containing 20 μM ATP and 5 μCi of [gamma-^{32}P]ATP. After 5 or 20 min at 30°C, the reaction was terminated by the addition of 2.5x Laemlli sample buffer, and applied to 10% SDS-polyacrylamide gel. GST-Eno1 was visualized by CBB staining, and then, the gel was subjected to autoradiography.

Phosphorylation of Fgr_{KD} or FGR_{KD} by Csk was analyzed as follows. One μg of GST-Fgr_{KD} or GST-FGR_{KD} alone or with 10 ng of Csk were suspended in 15 μl of kinase buffer

[20 mM Hepes, pH 7.6, 10 mM MgCl2, 1 mM beta-glycerophosphate, 2.5 mM NaF, 1 mM Na3VO4, 1 mM DTT] containing 20 μM ATP and 5 μCi of [γ-^{32}P]ATP. After 20 min at 30°C, the reaction was terminated by the addition of 2.5x Laemlli sample buffer and applied to 8.5% SDS-polyacrylamide gel. GST-Fgr_{KD} and GST-FGR_{KD} were visualized by CBB staining, and then, the gel was subjected to autoradiography.

Plasmids. For overexpression experiments in cultured cells, the constructs were made in house. Briefly, bone and bone marrow cDNA were synthesized using RNA from whole femur of wild-type C3HeB/FeJ and *Ali18/Ali18* mice, and full coding *Fgr* cDNA was amplified using a pair of PCR primers (Fgr_rt2L, 5'-GTCTGTGGGGGCATCTGG and Fgr_rt2R, 5'-GGGATTGGCTGATGCCCAGT). The PCR products were cloned into the pTARGET vector (Promega). The insert *Fgr* coding sequences of wild type (w21) and p.Asp502Gly (A14R5) were confirmed by Sanger sequencing.

For construction of the expression plasmids of mouse *Csk*, *Fgr* (wt) and *Fgr* (mut, p.Asp502Gly), the corresponding entire coding regions were amplified by PCR using the following oligonucleotide: CSK-SpeIATG_L1, 5'-

TTCAACTAGTATGTCFGGCAATACAGGCCG; Csk-TGAHindIII, 5'-TTAAAGCTTTCACAGGTGCAGCTCATGGGT; Fgr_SpeI-L1, 5'-TTCAACTAGTAGGGCTGTGTGTTCTGCA; FgrTGA_HindII-R2, 5'-TTAAAGCTTCTATGTCTGGTCTCCAGGCTG. PCR products were digested with Spe I and Hind III, and then cloned into the corresponding sites of pET49b (Novagen) using the TAKARA Ligation Kit. The insert *Fgr* sequence with no undesired (Ftw) and p.Asp502Gly mutations (FTA) and the *Csk* with no undesired mutations (2-2-2) were confirmed by Sanger sequencing. To repress autophosphorylation of *Fgr*, a p.Lys279Met (K279M) mutation was introduced using the following oligonucleotides: Fgr-K279M_L1, 5'-CAGTGATGACGCTGAAGCCGGGCA; Fgr-K279M_R1, 5'-CAGCGTCATCACTGCCACCTTTGTGC. The insert sequence with the desired mutation was confirmed by Sanger sequencing (Ftw_KM1 and FTA_KM4).

For kinase assays using human *FGR* mutations, the ORF clone (OHu28536D) was purchased from Genscript Japan. The coding region of *FGR* was cloned into pGEX4T2 (GE Healthcare). The p.P525S and p.R118W mutations were introduced using the following oligonucleotides: hFGR3'-XhoI_R2-, 5'-

GCCGCTCGAGTCTATGTCTGATCCCCGGACTGG; FGR_R118W_L1, 5'-GGAGGCTTGGTCTCTCAGCTC; FGR_R118W_R1, 5'-TGACCACCCTCCGAACCAGAGA. For phosphorylation by Csk, a kinase dead mutation was introduced into above constructs using the following oligonucleotides: FGR_K291M_L1, 5'-GGTGATGACGCTGAAGCCGGGCA and FGR_K291M_R1, 5'-GTGATTCCACCGCACTACTGCGAC.

For construction of the expression plasmid for mouse enolase 1 from amino acid 3 to 92, PCR product of the corresponding region was cloned into the *Eco*RI and *Xho*I sites of pGEX-4T-2 using the following oligonucleotides: mEno1-147FE (*Eco*RI), 5'-ATTCGCCATGTGAATTCTCAGGAT-3'; mEno1-447RX (*Xho*I), 5'-GTCCATCTCGAGCATCAGCTTGT-3'.

In genome editing of *Ali18* mice, to introduce various mutations around exon 3 of the *Fgr* gene in *Ali18* mice, we used the CRISPR/Cas9 system using the pX330-U6-Chimeric_BB-CBh-hSPCas9 vector(11)(https:adgene.org/42230). Two guided RNA sequences, f-gRNA1 (f-gRNA1_L: 5'-CACCGTTCTTCAGCCGTTTGGCTC and f-gRNA1_R: 5'- AAACGAGCCAAACGGCTGAAGAAC) and f-gRNA2 (f-gRNA2_L: 5'-

CACCTGCATCAGGGCATCTGGAAT, and f-gRNA2_R:

AAACATTCCAGATGCCCTGATGCA), were cloned into the Bbs I site of the pX330 vector according to the Addgene's CRISPR guide (https://www.addgene.org/crispr/guide/).

Structural modeling and molecular dynamics simulations. The three-dimensional structure of the active FGR (residues 77-529) was modeled off the crystal structure of the human tyrosine kinase c-SRC (PDB:1FMK (12); 74% sequence identity) using MODELLER 9.14 (13). The resultant model superimposed well with the template and had an RSMD of 0.2 A over 410 Ca atoms. The inactive FGR structure was modeled using the inactive c-SRC (PDB:1Y57) (4) structure as a template. The resultant model had an RSMD of 0.2A over 358 Ca atoms. *In silico* mutagenesis was performed in PyMOL (Schrödinger Corporation). Charges and hydrogen atoms were added to the wild-type and mutant FGR model using PDB2PQR (14). Electrostatic potentials were calculated using APBS (15). Protein and solvent dielectric constants were set to 2.0 and 78.0, respectively. PyMOL generated all structural figures (Schrödinger Corporation).

We performed all-atom molecular dynamics (MD) simulations of wild-type and p.Arg118Trp FGR SH3 domain models using YASARA 15.7.25 software package (16). The system was then subjected to 250 ps restrained equilibration simulation in the NVT ensemble. Temperature was set to 298K and the system was solvated in water with 0.9% NaCl and a pH of 7.4. The AMBER14 (17) all-atom force field was then run for 100 ns with trajectory conformations saved every 250 ps. Analysis were performed using the YASARA macros md analyze.mcr and md analyzers.mcr.

Figure S1

A


Mouse (mm10)
chr4
chr4:133,000,243-133,000,344
Go
qA1 qA2 qA3 qA4 qA5 qB1 qB2 qB3 qC1 qC3 qC4 qC5 qC6 qC7 qD1 qD2.2 qD3 qE1 qE2
A133000294G
133,000,260 bp
133,000,280 bp
133,000,300 bp
133,000,320 bp
133,000,340 bp
0781-2_Alil8_sort.bam Coverage
0781-2_Alil8_sort.bam
0736-1_AGA3_sort.bam Coverag
0736-1_AGA3_sort.bam
Sequence
Refseq genes
Fgr
6 tracks loaded
chr4:133,000,339
282M of 640M

Figure S1

B


IGV
File Genomes View Tracks Regions Tools GenomeSpace Help
Mouse (mm10)
chr4
chr4:133,543,370-133,543,494
Go
A133543428G
133,543,380 bp
133,543,400 bp
133,543,420 bp
133,543,440 bp
133,543,460 bp
133,543,480 bp
0781-2_Alil8_sort.bam Coverage
0781-2_Alil8_sort.bam
0736-1_AGA3_sort.bam Coverag
0736-1_AGA3_sort.bam
Sequence
Refseq genes
6 tracks loaded
chr4:133,543,413
286M of 311M

Figure S1

C


IGV
File Genomes View Tracks Regions Tools GenomeSpace Help
Mouse (mm10)
chr4
chr4:133,705,245-133,705,369
Go
A133705306G
126 bp
133,705,260 bp
133,705,280 bp
133,705,300 bp
133,705,320 bp
133,705,340 bp
133,705,360 bp
0781-2_AliI8_sort.bam Coverage
0781-2_AliI8_sort.bam
0736-1_AGA3_sort.bam Coverag
0736-1_AGA3_sort.bam
Sequence
Refseq genes
6 tracks loaded
chr4:133,705,332
595M of 812M

Figure S1

D

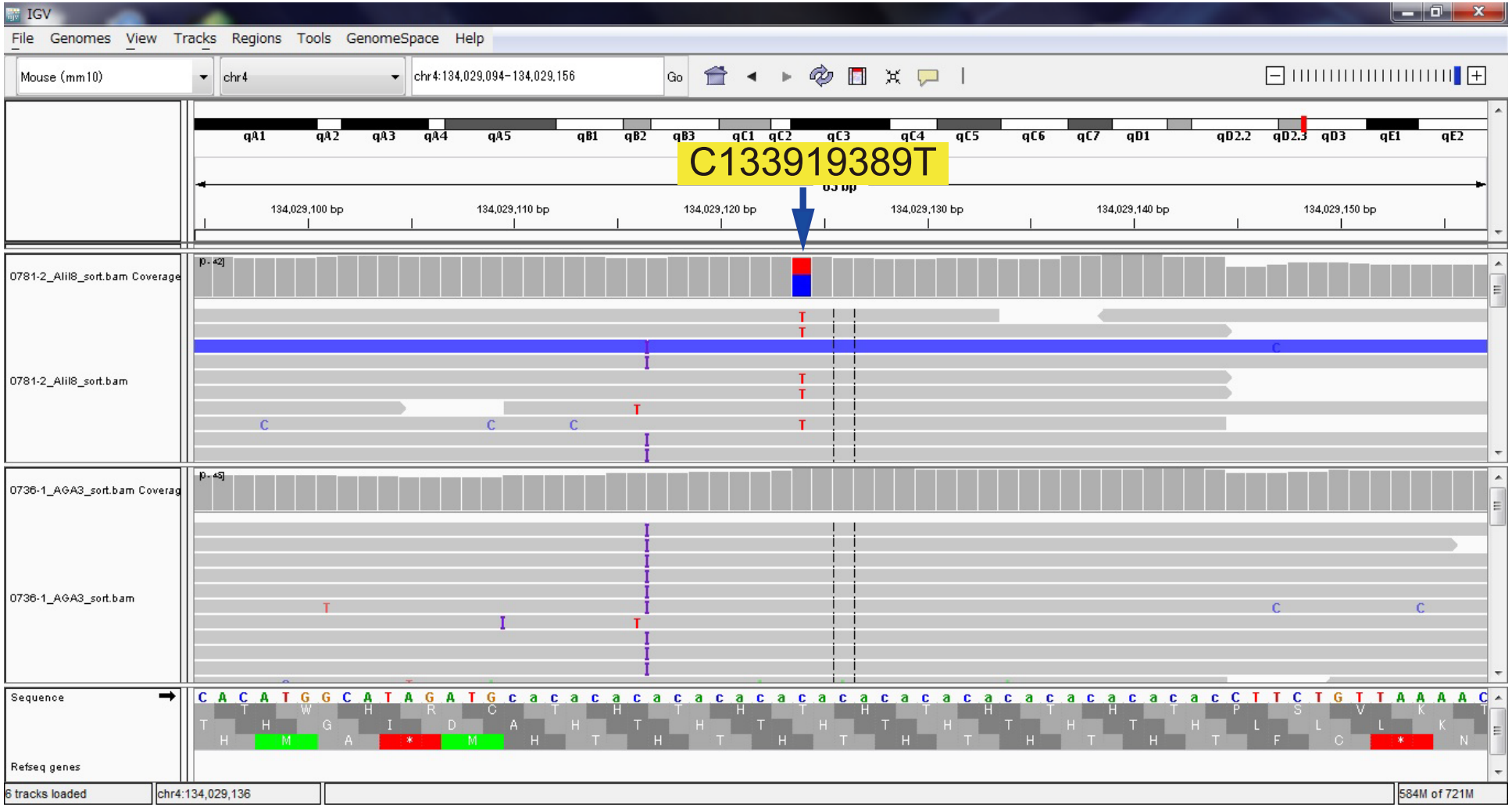
IGV
File Genomes View Tracks Regions Tools GenomeSpace Help
Mouse (mm10)
chr4
chr4:134,029,094-134,029,156
Go
C133919389T
134,029,100 bp
134,029,110 bp
134,029,120 bp
134,029,130 bp
134,029,140 bp
134,029,150 bp
0781-2_Alil8_sort.bam Coverage
0781-2_Alil8_sort.bam
0736-1_AGA3_sort.bam Coverag
0736-1_AGA3_sort.bam
Sequence
Refseq genes
6 tracks loaded
chr4:134,029,136
584M of 721M

Figure S2

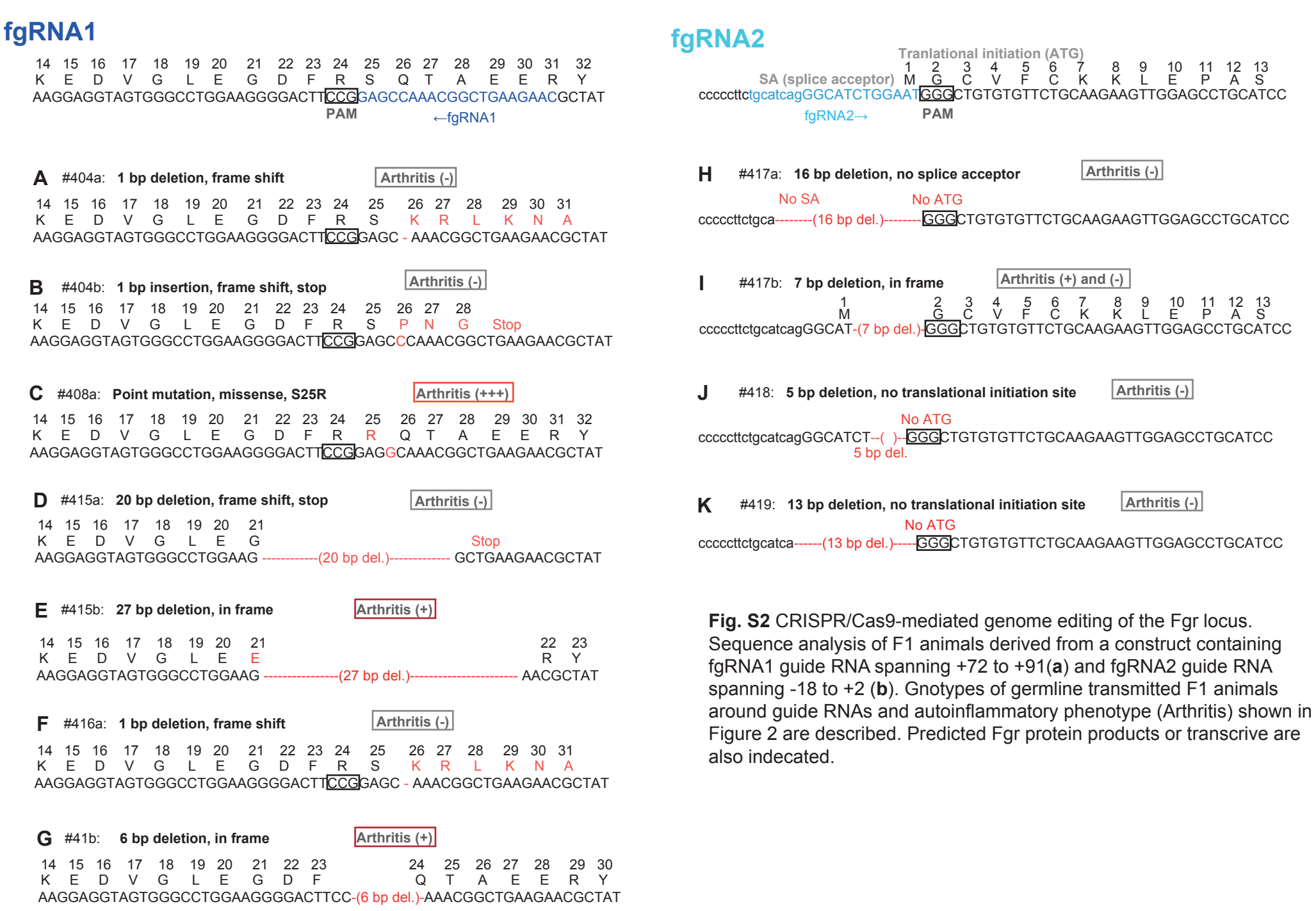

Fig. S2 CRISPR/Cas9-mediated genome editing of the Fgr locus. Sequence analysis of F1 animals derived from a construct containing fgRNA1 guide RNA spanning +72 to +91(**a**) and fgRNA2 guide RNA spanning -18 to +2 (**b**). Gnotypes of germline transmitted F1 animals around guide RNAs and autoinflammatory phenotype (Arthritis) shown in Figure 2 are described. Predicted Fgr protein products or transcrive are also indecated.

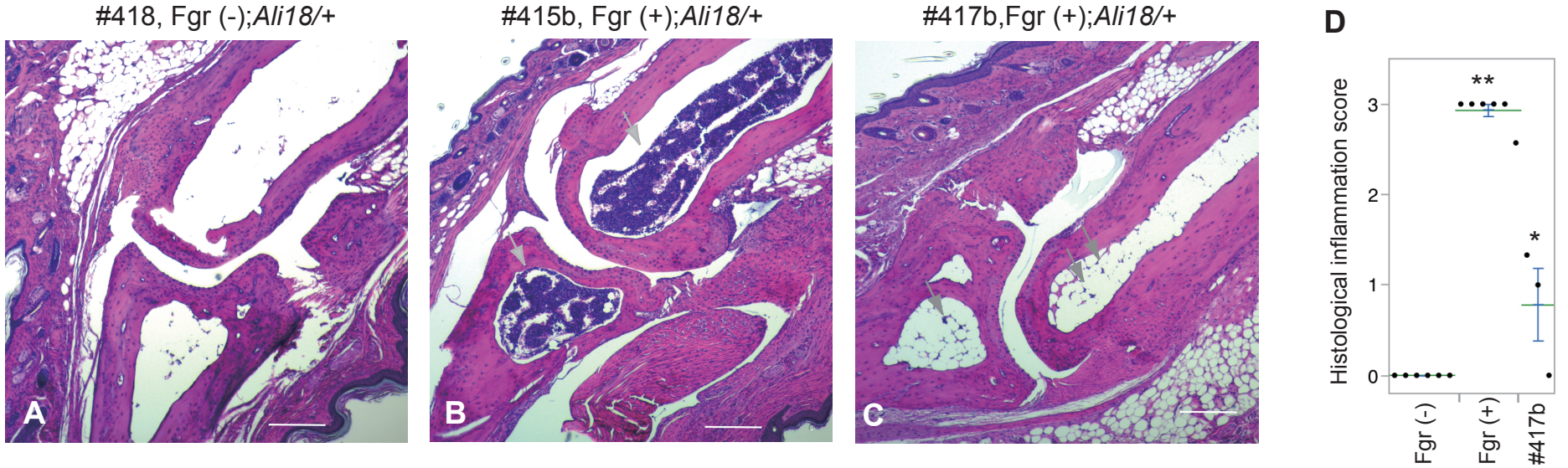

Fig. S3 Histological analysis of peripheral paws of F1 mice with genetic modification by CRISPR/*Cas9*-mediated genome editing of the *Fgr* locus. (A) Hematoxylin and eosin (HE) stained sections of the joint between talus and navicular bone from #418 strain F1 mice are indicated. The #418 strain has a deleterious mutation of *Fgr*. Other strains with the same mutation type are grouped as Fgr (-). (B) HE stained sections of the joint between talus and navicular bone from #415 F1 mice are indicated. The #415 has a missense (in flame) mutation of *Fgr*. Other strains with in flame mutation type are grouped as Fgr (+). Inflammtory cells in bone marrow are indicated by arrows. (C) HE stained sections of the joint between talus and navicular bone from #417 F1 mice. #417 has deletion in exon 3 but resuled in intact Fgr. #417 F1 mice show a partial inflammatory paw phenotype. (D) Histological scoring for severity of bone inflammation was performed on peripheral paws of F1 mice. Fgr (+) (n = 6), Fgr(-) (n = 6), and #417b (n = 3) were used. Average bar (x axis) and SE bar (y axis) are shown. *: $P < 0.005$; **: $P < 0.0001$ by paird *t*-tests.

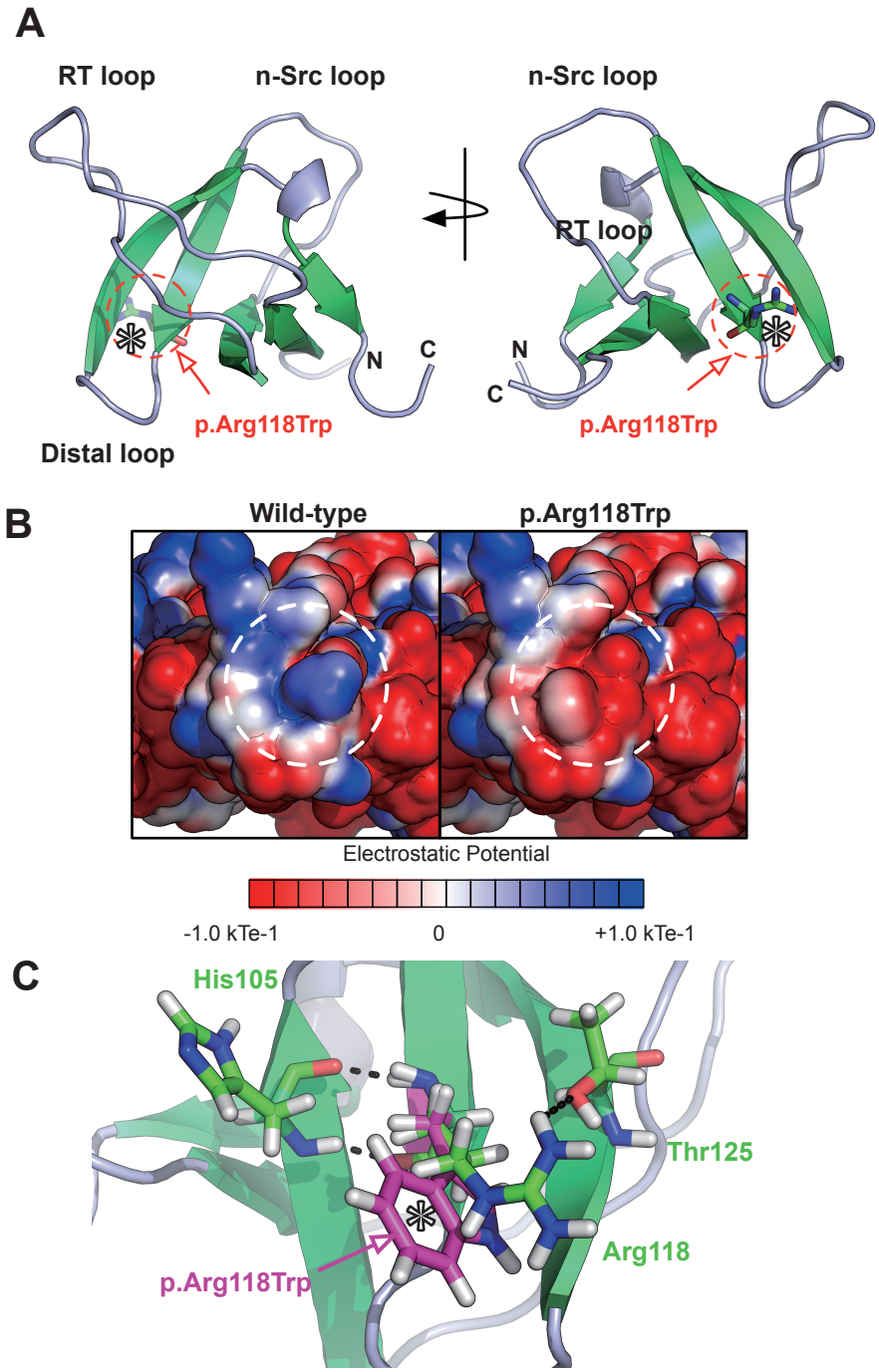

Fig. S4. Predicted mechanism of the human FGR p.Arg118Trp mutation.

(**A**) Structural model of the FGR SH3 domain generated using C-SRC as a template (PDB: 1FMK). The p.Arg118Trp mutation is located in a beta strand near the distal loop of the SH3 domain. (**B**) Wild-type and p.Arg118Trp electrostatic potentials were analyzed using APBS. The p.Arg118Trp mutation leads to a loss of positive charge. (**C**) Superimposition of the final structures obtained during a 100-ns simulation. The p.Arg118Trp disrupts a hydrogen bonding interaction with the neighboring Thr125 residue. Asterisk indecates amino acid substitution.

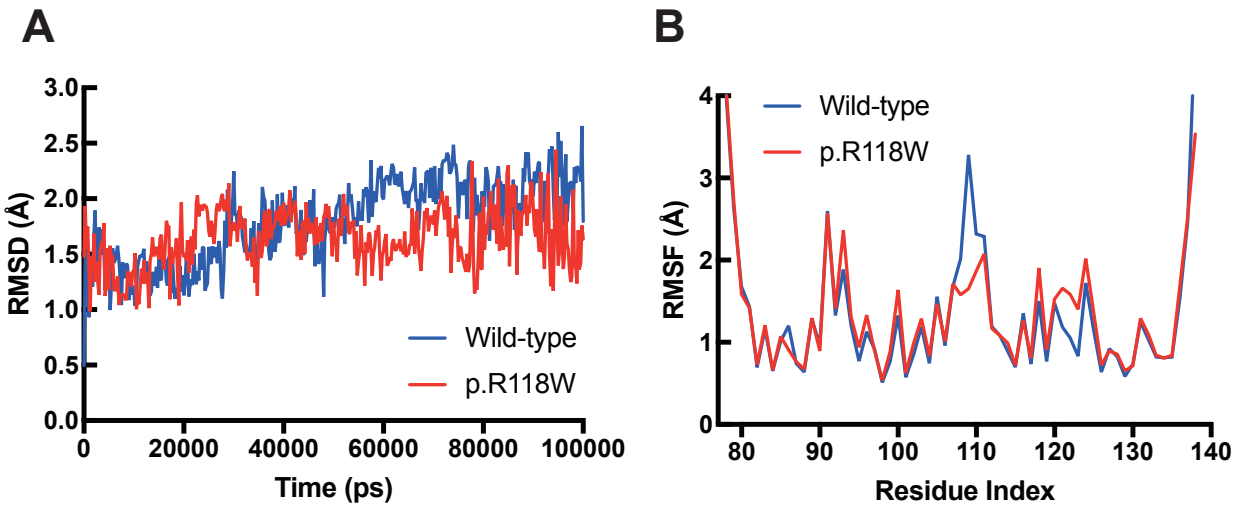

Fig. S5 Molecular dynamics simulations of the wild-type and p.Arg118Trp FGR SH3 domain. (**A**) Both wild-type and p.Arg118Trp SH3 domain models were analyzed using all-atom molecular dynamics (MD) simulations (100-ns each). Root mean square deviation (RMSD) values of the FGR SH3 domain backbone atoms were calculated relative to the initial minimized structure throughout the simulation. Both the wild-type and p.Arg118Trp FGR reached equilibrium at around 30-ns of simulation. (**B**) Further analysis of root mean square fluctuation (RMSF) versus the protein residue for the wild-type and p.Arg118Trp FGR SH3 domains is illustrated. Both the wild-type and mutant SH3 domains possess the similar RMSF distributions.

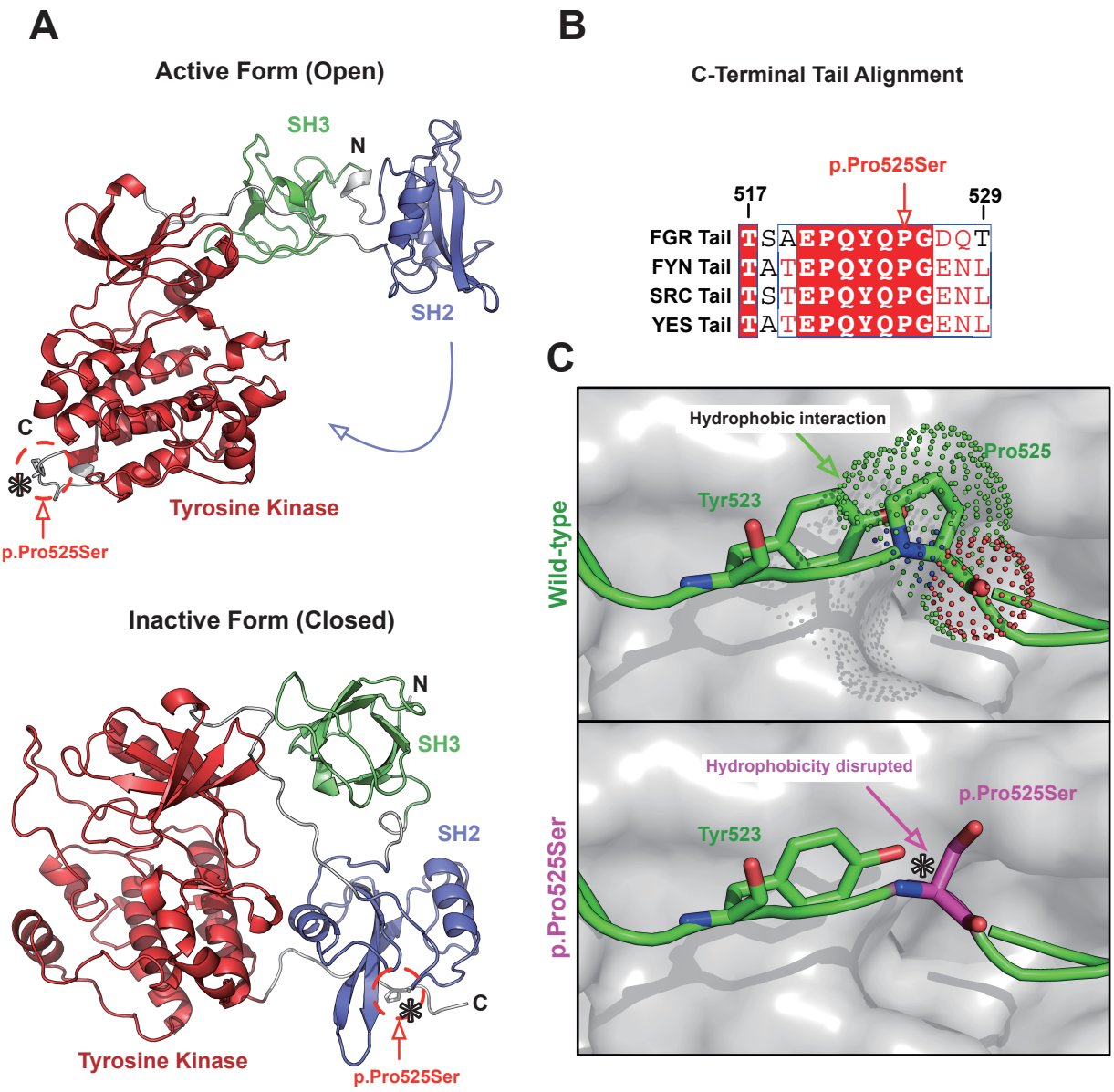

Fig. S6. Predicted mechanism of the human FGR p.Pro525Ser mutation.

(**A**) (Up) Structural model of the active form of FGR modeled off the crystal structure of the human tyrosine kinase C-SRC (PDB: 1Y57). Phosphorylation of Tyr523 by CSK leads to a domain rearrangement that facilitates auto-phosphorylation at Tyr412. The p.Pro525Ser mutation is located at a C-terminal tail that interacts with the SH2 domain. (Down) Structural model of the inactive FGR form modeled off the crystal structure of the human tyrosine kinase C-SRC (PDB: 1FMK). (**B**) Multiple sequence alignment of C-terminal tails from FGR and several other human tyrosine kinases: FYN, SRC, and YES. Multiple sequence alignments were performed using Geneious R9 and visualized in ESPript 3. The p.Pro525 residue is conserved across several tyrosine kinases. (**C**) Close-up of the C-terminal tail of the inactive FGR. (Up) The p.Pro525 residue forms a hydrophobic interaction that binds to the SH2 domain. (Down) The p.Pro525Ser mutation disrupts this hydrophobic interaction and leaves Tyr523 exposed for potential phosphorylation and dephosphorylation. Asterisk indecates amino acid substitution.

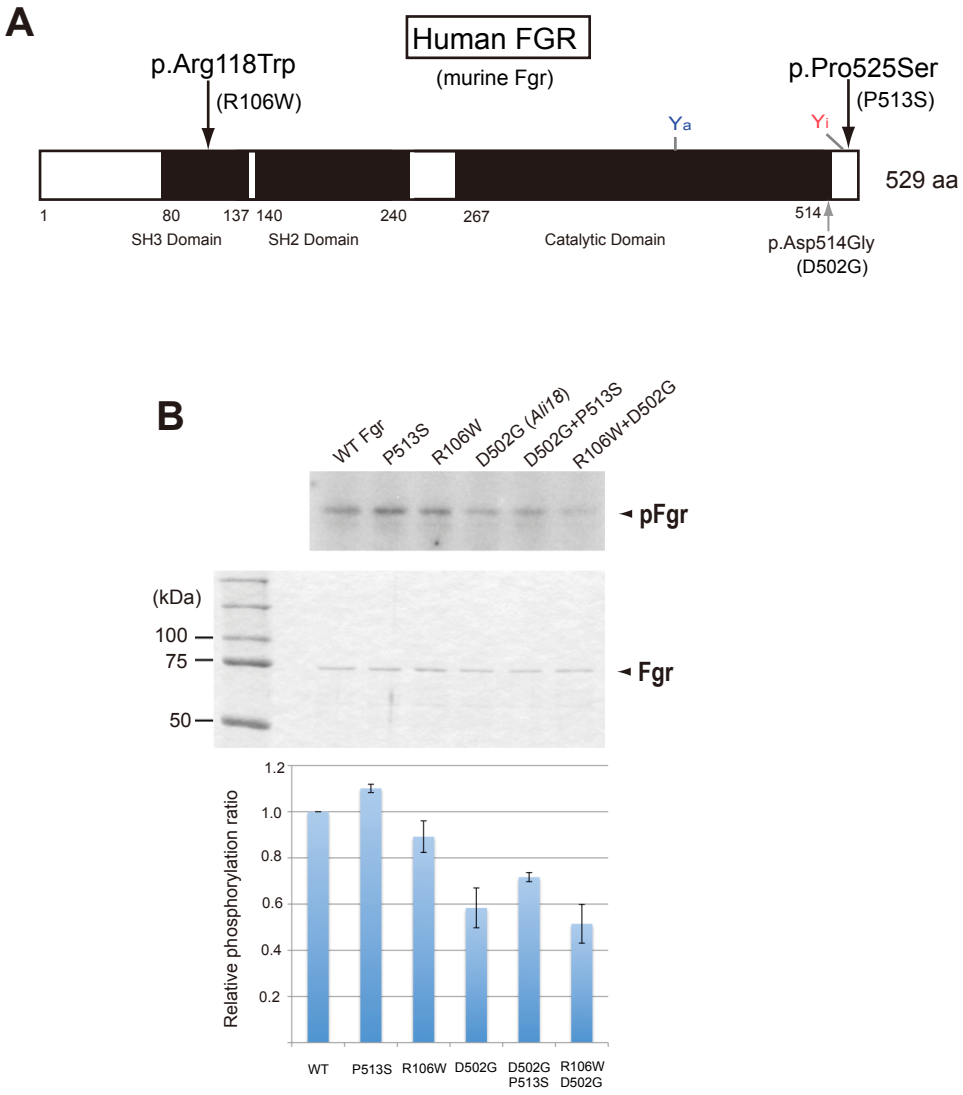

Fig. S7. C-terminal phosphorylation of murin Fgr corresponding to human mutations.(A) Schematic diagram of the amino acid changes caused by human FGR coding mutation found in CRMO. Corresponding murine Fgr mutations were indicated in parentheses. Ya and Yi indicate the autophosphorylation site (412 tyrosine) and the C-terminal regulatory phosphorylation site (523 tyrosine), respectively. (B) Phosphorylation of mutant murine Fgr proteins corresponding human FGR coding mutations by Csk. All Fgr proteins also contain the KD mutation (p.Lys279Met). (top) Phosphorylated Fgr proteins by Csk are shown. The proteins used for kinase assays were fractionated by SDS-PAGE and stained by Coomassie brilliant blue (middle). Experiments are independently triplicated.

Table S1 Genetic mapping of the *Ali18* critical region using in house microsattelite markers

ID	tag	D4Mit12	D4Mit203	D4Neu12	D4Neu6	D4Mit204	D4Mit71	D4Mit339	D4Neu9	D4Mit134	D4Mit54	D4Mit68
10128572	9	B/B	B/B	C/C	C/C	C/C	C/C	C/C	C/C	C/C	C/C	C/C
10135632	69	B/B	B/B	B/B	C/B	C/B	C/B	C/B	C/B	C/B	C/B	C/B
10138700	24	C/B	C/B	C/B	C/B	C/B	C/B	C/B	C/B	B/B	B/B	B/B

B/B: Homozygous for C57BL/6J; C/C: Homozygous for C3HeB/FeJ; C/B: Heterozugous of C3HeB/FeJ and C57BL/6J

Table S2　Summary of Fgr coding variants induced by the CRISPR/Cas9 system in *Ali18* mice

Strain	guide RNA	Nucleotide change	Protein change	Mutation type	Fgr products (predicted)	Fgr haplotype	Generation (genotype)	Inheritance	Swollen paws
#404a	fgRNA1	c.76delC	p.Gln26fs*35	frame shift, nonsense	−	p.Asp502Gly	F1 (*Ali18*/+)	5	0
#404b	fgRNA1	c.75_76insC	p.Gln26fs*4	frame shift, nonsense	−	p.Asp502Gly	F1 (*Ali18*/+)	8	0
#408a	fgRNA1	c.75C>G	p.S25R	missense	+	p.Asp502Gly	F1 (*Ali18*/+)	6	6
#408b	fgRNA1	c.75_76del	p.Ser25fs*4	frame shift, nonsense	−	p.Asp502Gly	F1 (*Ali18*/+)	2	0
#415a	fgRNA1	c.62_81del	p.22fs*2	frame shift, nonsense	−	p.Asp502Gly	F1 (*Ali18*/+)	10	0
#415b	fgRNA1	c.62_88del	p.Gly21_Glu30del	deletion	+	p.Asp502Gly	F1 (*Ali18*/+)	4	4
#416a	fgRNA1	c.76delC	p.Gln26fs*35	frame shift, nonsense	−	p.Asp502Gly	F1 (*Ali18*/+)	4	0
#416b	fgRNA1	c.71_76del	p.Arg24Gln25_26del	missense, deletion	+	p.Asp502Gly	F1 (*Ali18*/+)	1	1
#417a	fgRNA2	c.(−14)_(−3)del	none	SA and 5'UTR deletion	−	p.Asp502Gly	F1 (*Ali18*/+)	6	0
#417b	fgRNA2	c.(−5)_2del	none	5'UTR deletion, synonymus	+	p.Asp502Gly	F1 (*Ali18*/+)	9	4
#418	fgRNA2	c.(−3)_2del	p.Met1del	ATG deletion	−	p.Asp502Gly	F1 (*Ali18*/+)	8	0
#419	fgRNA2	c.(−11)_2del	p.Met1del	SA and ATG deletion	−	p.Asp502Gly	F1 (*Ali18*/+)	5	0

Table S3: All exonic FGR variants found in the 99 CRMO probands

CHR	POS [hg19]	dbSNP ID	Proband	Inheritance	MAF (gnomAD)	REF	ALT	Effect [NM_005248]	Other variants*
1	27939005	rs191541855	A	paternal	0.00006457	A	G	3' UTR	n.d.
1	27939442	rs143850913	Case 2	unknown	0.000354	G	A	P525S	n.d.
1	27941096	rs757288230	B	paternal	0.000008164	TG	T	splice acceptor region §	n.d.
1	27941102	n/a	B	paternal	0	A	T	splice site region	n.d.
1	27942276	rs142998887	C, D, E	paternal/maternal	0.01402	G	A	D254=	n.d.
1	27942362	rs367996753	F, K	paternal	0.001112	G	T	splice site region	FBLIM1
1	27948132	rs2231870	G	maternal	0.003698	G	A	S122=	FBLIM1
1	27948146	rs774209795	Case1	de novo	0.00001218	G	A	R118W	n.d.
1	27952665	rs536321858	H	unknown	0	C	T	5' UTR	n.d.
1	27961658	n/a	I	paternal	0.0001617	G	A	5' UTR	n.d.
1	27961692	rs372572478	J	paternal	0.00006463	G	A	5' UTR	LPIN2

*: Coding variants in CRMO candidate genes which have been characterized. See Table S4 for further information. § : Deletion of 1st G in polypyrimidine tract.

Table S4: Missense variants in CRMO candidate genes found in probands with FGR coding variants.

Gene	CHR	POS [hg19]	dbSNP ID	Protein change	MAF (gnomAD)	Proband	Inheritance
LPIN2	18	2920361	rs201160155	C874F	0.0012	J	maternal
FBLIM1	1	16101332	rs114077715	G311R	0.01954	K	maternal
FBLIM1	1	16101332	rs114077715	G311R	0.01954	G	paternal

Supplementary Table S5: Scoring of FGR proteins by *in silico* predictors

FGR variant	PROVEAN	CADD	SIFT	POLYPHEN2
R118W	-5.015	26.3	D	D
P525S	-2.716	18.2	D	P

References for SI reference citations

1. Toral MA, *et al.* (2017) Structural modeling of a novel SLC38A8 mutation that causes foveal hypoplasia. *Mol Genet Genomic Med* 5(3):202-209.
2. Cox AJ, *et al.* (2017) Recessive coding and regulatory mutations in FBLIM1 underlie the pathogenesis of chronic recurrent multifocal osteomyelitis (CRMO). *PLoS One* 12(3):e0169687.
3. Moshfegh Y, *et al.* (2016) BESTROPHIN1 mutations cause defective chloride conductance in patient stem cell-derived RPE. *Hum Mol Genet* 25(13):2672-2680.
4. Cowan-Jacob SW, *et al.* (2005) The crystal structure of a c-Src complex in an active conformation suggests possible steps in c-Src activation. *Structure* 13(6):861-871.
5. Kaneko T, Li L, & Li SS (2008) The SH3 domain--a family of versatile peptide- and protein-recognition module. *Front Biosci* 13:4938-4952.
6. Waksman G, Shoelson SE, Pant N, Cowburn D, & Kuriyan J (1993) Binding of a high affinity phosphotyrosyl peptide to the Src SH2 domain: crystal structures of the complexed and peptide-free forms. *Cell* 72(5):779-790.
7. Dietrich W, *et al.* (1992) A genetic map of the mouse suitable for typing intraspecific crosses. *Genetics* 131(2):423-447.
8. Dietrich WF, *et al.* (1994) A genetic map of the mouse with 4,006 simple sequence length polymorphisms. *Nat Genet* 7(2 Spec No):220-245.
9. Abe K, Fuchs H, Lisse T, Hans W, & Hrabe de Angelis M (2006) New ENU-induced semidominant mutation, Ali18, causes inflammatory arthritis, dermatitis, and osteoporosis in the mouse. *Mamm Genome* 17(9):915-926.
10. Bagheri-Yarmand R, *et al.* (2001) Etk/Bmx tyrosine kinase activates Pak1 and regulates tumorigenicity of breast cancer cells. *J Biol Chem* 276(31):29403-29409.
11. Cong L, *et al.* (2013) Multiplex genome engineering using CRISPR/Cas systems. *Science* 339(6121):819-823.
12. Xu W, Harrison SC, & Eck MJ (1997) Three-dimensional structure of the tyrosine kinase c-Src. *Nature* 385(6617):595-602.

13. Webb B & Sali A (2016) Comparative Protein Structure Modeling Using MODELLER. *Curr Protoc Protein Sci* 86:2 9 1-2 9 37.
14. Dolinsky TJ, Nielsen JE, McCammon JA, & Baker NA (2004) PDB2PQR: an automated pipeline for the setup of Poisson-Boltzmann electrostatics calculations. *Nucleic Acids Res* 32(Web Server issue):W665-667.
15. Konecny R, Baker NA, & McCammon JA (2012) iAPBS: a programming interface to Adaptive Poisson-Boltzmann Solver (APBS). *Comput Sci Discov* 5(1).
16. Krieger E & Vriend G (2014) YASARA View - molecular graphics for all devices - from smartphones to workstations. *Bioinformatics* 30(20):2981-2982.
17. O'Hare T*, et al.* (2004) Inhibition of wild-type and mutant Bcr-Abl by AP23464, a potent ATP-based oncogenic protein kinase inhibitor: implications for CML. *Blood* 104(8):2532-2539.